Cloud-Property Retrieval Using Merged HIRS and AVHRR Data

BRYAN A. BAUM, BRUCE A. WIELICKI, AND PATRICK MINNIS

Atmospheric Sciences Division, NASA Langley Research Center, Hampton, Virginia

LINDSAY PARKER

Lockheed Engineering and Sciences Corporation, Hampton, Virginia

(Manuscript received 28 January 1991, in final form 28 July 1991)

ABSTRACT

A technique is developed that uses a multispectral, multiresolution (MSMR) method to improve the overall retrieval of mid- to high-level cloud properties by combining HIRS sounding channel data with higher spatial resolution AVHRR radiometric data collocated with the HIRS footprint. Cirrus cloud radiative and physical properties are determined using satellite data, surface-based measurements provided by rawinsondes and lidar, and aircraft-based lidar data collected during the First ISCCP (International Satellite Cloud Climatology Program) Regional Experiment (FIRE) in Wisconsin during the months of October and November 1986. HIRS cloud-height retrievals are compared to ground-based lidar and aircraft lidar when possible. Retrieved cloud heights are found to have close agreement with lidar for thin cloud, but are higher than lidar for optically thick cloud. The fact that the retrieved cloud height is higher than lidar for optically thick cloud is probably due to the attenuation of the lidar signal before the signal reaches through the cloud, while the satellite is viewing the cloud from above. AVHRR visible (0.63-μm) and infrared (11-μm) radiances are analyzed to determine the cloud emittances and reflectances collocated with each HIRS pixel. The bidirectional reflectances from the AVHRR visible-channel data are corrected for solar direct and diffuse surface reflection to isolate the cloud reflectance. The individual AVHRR pixel emittances are calculated using the cloud-top temperature derived from the HIRS cloud-retrieval analysis. The results of the reflectance–emittance relationships derived in this fashion are compared to theoretical scattering model results for both water-droplet spheres and randomly oriented hexagonal ice crystals. It is found that the assumption of 10-μm water droplets is inadequate to describe the reflectance–emittance relationship for the ice clouds seen here. Use of this assumption would lead to lower cloud heights using the ISCCP approach. The theoretical results show that use of hexagonal ice-crystal phase functions could lead to much improved results for cloud retrieval algorithms using a bispectral approach.

1. Introduction

High-level cirrus clouds are recognized to have an important influence on the earth's climate. In general, cirrus are composed of nonspherical ice crystals having a wide range of sizes and shapes (e.g., Heymsfield and Platt 1984; Heymsfield 1975). Further, cirrus are often optically thin, resulting in a low visible reflectance and an infrared (IR) emittance of less than one. These properties of cirrus complicate their analysis and detection. Satellite cloud-retrieval algorithms attempt to infer such cloud properties as cloud fractional coverage, cloud-top height, cloud visible optical depth, and cloud infrared emittance. The large number of existing cloud retrieval algorithms, each typically inferring only one or two of the cloud properties, demonstrates the difficulty of assessing cloud physical properties. In this article, we derive an improved cloud retrieval technique for mid- and high-level clouds, that is, clouds above 3–4 km, for determining cloud height, cloud-top pressure, emittance, and cloud fractional coverage by using two instruments flown on the NOAA (National Oceanic and Atmospheric Administration) orbiting platforms, the High-Resolution Infrared Radiation Sounder (HIRS/2, henceforth HIRS) and the Advanced Very High-Resolution Radiometer (AVHRR).

Thin cirrus is difficult to identify on a satellite image using a visible channel because the cloud generally does not reflect much solar radiation. A cloud retrieval technique that tries to exploit the small difference in reflectivity between clear-sky conditions and the reflectivity due to the presence of cirrus is not optimal in this case. The presence of cirrus shows up much better on an infrared window channel image because the high cloud is radiating at a much lower temperature than the earth. Cloud-retrieval techniques that depend on an infrared window channel may run into problems if they make the assumption that the cloud has an emittance of one (the blackbody assumption). An alternative technique used in deriving cloud-top pressures

Corresponding author address: Dr. Bryan A. Baum, NASA Langley Research Center, Mail Stop 420, Hampton, VA 23665-5225.

for optically thin mid- and high-level clouds uses thermal IR sounding channels in the CO_2 15-μm absorption bands (Smith et al. 1970; Smith and Platt 1978; Chahine 1974). A new method developed here attempts to improve the ability of existing satellite radiometer algorithms to recover information on mid- and high-level clouds above 3–4 km by combining data from the HIRS and AVHRR instruments on the *NOAA-9* operational satellite. This combination of datasets leads to a much improved algorithm for the detection and analysis of cirrus clouds.

The present work continues efforts to measure and model the radiative properties of cirrus clouds using remote sensing techniques. Satellite radiance measurements from the *NOAA-9* platform, aircraft lidar, ground-based lidar, and rawindsonde data are used to examine cirrus radiative properties both over water and land surfaces. Section 2 gives an overview of the strategy used to analyze the merged AVHRR and HIRS radiometric data. Section 3 outlines the methods used to merge the HIRS and AVHRR datasets and to prepare a clear-sky albedo map for use in the reflectance–emittance calculations. Section 4 outlines the methods used to determine cloud properties. The results from both measured and theoretical calculations are presented in section 5, and the work is summarized in section 6.

2. Technique description

The thermal infrared channels on the HIRS instrument are used to derive cloud properties such as effective cloud amount [ϵA_{cld}, where ϵ is the emittance and A_{cld} is the cloud fractional coverage in the satellite field of view (FOV)] and cloud-top pressure P_{cld}. Emittance may be less than one. To derive these properties, the methodology uses a combination of radiances in the 15-μm CO_2 band and the 11-μm window channel.

In the 15-μm CO_2 band, there are seven channels spaced between 14.95 (channel 1) and 13.35 μm (channel 7), and each channel registers a different amount of CO_2 absorption. Each channel, therefore, is sensitive to a different level in the atmosphere. A channel that has its peak sounding level high in the atmosphere will not register the presence of any cloud well below that level, while high clouds will always appear in channels that have their sounding peak low in the atmosphere. With a knowledge of the temperature and humidity profiles and the profiles of such gases as water vapor (H_2O) and carbon dioxide (CO_2), the theoretical amount of upwelling infrared radiation can be calculated at any pressure level. The calculated upwelling infrared radiation used in conjunction with the measured satellite radiances then allows the computation of cloud pressure.

The 15-μm CO_2 sounding channels have been shown to derive accurate cloud altitude for optically thin high cloud (e.g., Wielicki and Coakley 1981; Wylie and Menzel 1989; Smith and Platt 1978; Smith and Frey 1990). The HIRS cloud algorithm eliminates the common assumptions of cloud-filled pixels and of cloud infrared emittance equal to one. The weaknesses of this cloud detection method are in its inability to accurately measure low-altitude cloudiness (Wielicki and Coakley 1981), its relatively low spatial resolution (approximately 18-km FOV at nadir), and the inability to separate ϵA_{cld} into individual emittance and cloud fractional cover values. The AVHRR spectral imager, on the other hand, has the atmospheric window channels and high spatial resolution (approximately 1.1 km at nadir) required to more accurately measure both low-level clouds and cloud fraction.

The technique developed here, a multispectral, multiresolution method (MSMR), takes advantage of both the higher-resolution AVHRR data and the HIRS sounding channel data to improve the overall retrieval of cloud properties. The AVHRR data are used to estimate A_{cld}, leading to an estimate of ϵ in a HIRS FOV, as discussed in section 4. The ability to estimate separately both cloud fraction and emittance is not possible with just the HIRS sounding channels. Since the cloud height can be determined accurately from HIRS sounding channel data, information may be obtained about the cloud's microphysical properties using the relationship between the cloud's reflectance and emittance. A reflectance–emittance relationship is used by the International Satellite Cloud Climatology Project (ISCCP) to retrieve cloud height. Results from the present study may be useful for the future improvement of ISCCP algorithms. Radiative transfer models are used to provide the reflectance–emittance relationships for several water and ice-crystal size distributions and are compared to the AVHRR–HIRS measurements in section 5. Reflectance–emittance relationships depend both on particle size and particle shape (Wielicki et al. 1990). Particle size affects the ratio of visible to infrared optical depth for radii less than about 30 μm. Particle shape affects the visible wavelength scattering phase function.

The MSMR algorithm is tested using data collected from ground stations and from the AVHRR and HIRS instruments aboard the *NOAA-9* operational satellite during the First ISCCP Regional Experiment (FIRE) in Wisconsin during the months of October and November 1986. Rawinsonde-derived temperature and relative humidity profiles are used to calculate clear-sky radiances. Cloud properties are validated using the available lidar soundings from three surface sites in Wisconsin.

3. Data

a. HIRS and AVHRR radiances

The HIRS instrument measures radiances at 19 infrared channels and 1 visible channel. Raw HIRS counts are converted to radiance using the nominal

TABLE 1. *NOAA-9* HIRS and AVHRR channels and spectral bandwidths used in this study.

Instrument	Channel	Bandwidth (μm)
HIRS	5	14.06–14.38
HIRS	6	13.50–13.80
HIRS	7	13.20–13.49
HIRS	8	10.93–11.35
AVHRR	1	0.57–0.70
AVHRR	4	10.33–11.25

count conversion coefficients provided with the data. The AVHRR has five channels, consisting of two visible channels and three infrared channels. The AVHRR 10-bit data from the two visible channels are converted to radiance using the calibration coefficients provided by Whitlock et al. (1990). Infrared channel counts are converted to radiance using the nominal AVHRR thermal calibration coefficients (Kidwell 1986). The HIRS and AVHRR channels used in this study are summarized in Table 1.

b. *Merging HIRS and AVHRR data*

In the following discussion on collocating HIRS and AVHRR data, it is important to consider the way the data will be used. The HIRS sounding channel data are used to calculate cloud pressure P_{cld} and thereby determine the 11-μm cloud radiance that would be emitted by an overcast black cloud at P_{cld}. The HIRS-derived 11-μm black-cloud radiance is used in turn to calculate the AVHRR pixel 11-μm emittances. When the AVHRR and HIRS data are used in this fashion, it is not critical to have the AVHRR FOV data exactly collocated with the larger HIRS FOV. The AVHRR data should come, however, from a region that is close to the HIRS FOV.

The mapping of 1.1-km AVHRR pixels into the larger HIRS FOV is performed for the FIRE intensive field observation (IFO) region between 42° and 47°N and between 86.5° and 92°W. The size of each HIRS pixel saved in the scan line varies because of the elongation of the pixel with increasing viewing angle. Near nadir, the HIRS footprint is approximately 18 km (Kidwell 1986). In this study, the HIRS FOV is modeled as a square box near nadir. The same number of AVHRR pixels are saved along the scan line for each HIRS FOV, but the number of pixels saved in the cross-track direction varies with the viewing angle. At either edge of the scan line, the HIRS footprint is modeled as a 30-km × 58-km rectangle in the absence of information on the point-spread function. In reality, the areal size of the footprint increases with the viewing angle and tends to have an elliptical form due to the curvature of the earth. However, modeling the HIRS footprint any differently would have no effect on the calculation of individual AVHRR pixel emittances, since the AVHRR pixel emittances are calculated using the HIRS-derived cloud height. There are approximately 250 AVHRR pixels collocated with a HIRS FOV at nadir. Toward the edge of the HIRS scan line, the number of collocated AVHRR pixels increases to more than 400. All AVHRR pixels located within a given HIRS pixel are grouped and associated with the HIRS pixel. Only a sampling of the collocated AVHRR data is shown in the reflectance–emittance figures presented later in the study. Further discussion of the possible errors in collocating AVHRR with HIRS is detailed in the error analysis in section 5e.

The mapping process is shown schematically in Fig. 1 and shows the nature of the HIRS scanning pattern for a near nadir view. Due to the nature of the HIRS instrument, there is approximately a 40–60-km gap between HIRS pixels along a scan line at nadir and approximately a 30–40-km gap between scan lines. Toward the edge of a scan line, the gap between consecutive HIRS pixels decreases as the HIRS pixels get larger, but there remains a gap between scan lines.

Both the HIRS and AVHRR instruments aboard the *NOAA-9* satellite have 11-μm window channels. Since the HIRS window channel 8 is spectrally narrower than the comparable AVHRR channel 4, information regarding possible errors in combining the data is required. To ensure compatability, the HIRS window channel brightness temperature is compared with the average (channel 4) brightness temperature of all AVHRR pixels that fall within each HIRS footprint. This test serves as a check both for the accuracy of the AVHRR–HIRS pixel matching and for the assumptions inherent in combining data from the two instruments.

Figure 2 gives the result of such a comparison for the composite clear-sky map derived from the relatively clear days of 18 and 19 October 1986. For clear-sky conditions, the mean and standard deviation of the difference between the HIRS 11-μm brightness temperature and the average AVHRR 11-μm brightness temperature of the collocated pixels is −0.7 and 1 K, respectively.

A radiative transfer calculation was performed to simulate the spectral response of the 11-μm channels

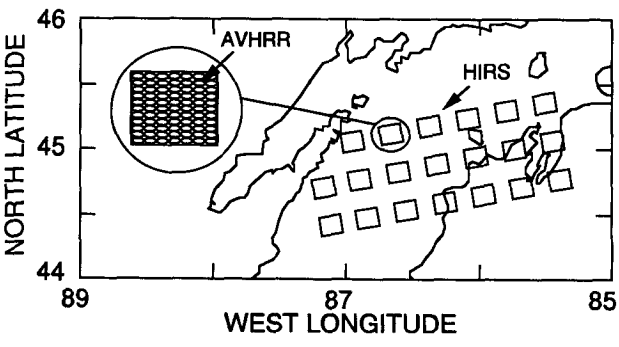

FIG. 1. Schematic of HIRS–AVHRR collocation process.

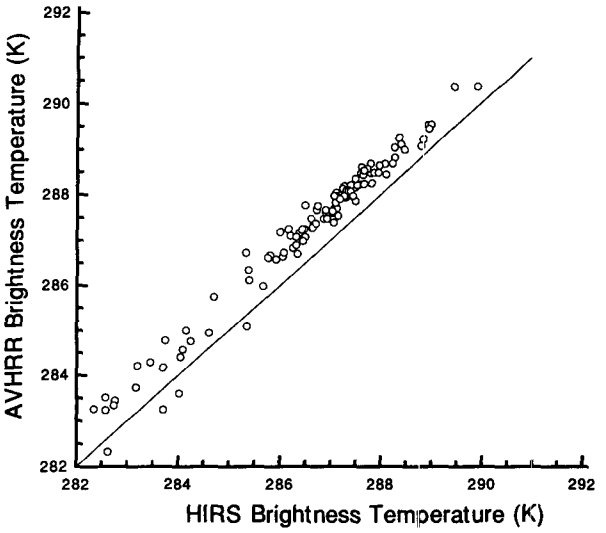

FIG. 2. Comparison of AVHRR and HIRS 11-μm channel brightness temperatures for clear conditions on 18 and 19 October 1986.

of the *NOAA-9* AVHRR and HIRS instruments. The results of these calculations indicate that the AVHRR 11-μm brightness temperature will be approximately 1.0 K warmer than the 11-μm HIRS brightness temperature. This agrees well with our data and does not indicate the presence of either collocation problems or radiometric calibration problems.

A comparison of AVHRR and HIRS 11-μm brightness temperatures is shown in Fig. 3 for a partially cloudy scene on 2 November 1986 at 2005 UTC. The mean and standard deviation of the difference between the HIRS 11-μm brightness temperature and the average AVHRR 11-μm brightness temperature of the collocated pixels is -1.0 and 1.2 K, respectively. This shows that for a wide range of radiating temperatures (290–220 K), the HIRS 11-μm brightness temperature is approximately 1 K lower than the average AVHRR 11-μm brightness temperature of the collocated pixels. For this reason, a 1.0-K difference in brightness temperatures is used when converting a HIRS 11-μm brightness temperature to an AVHRR 11-μm brightness temperature. In order to convert a HIRS 11-μm radiance to the equivalent AVHRR 11-μm radiance, the following procedure is used:

1) Convert HIRS 11-μm spectral radiance to brightness temperature.
2) Offset the HIRS brightness temperature by 1 K.
3) Convert adjusted brightness temperature in previous step to AVHRR spectral radiance.

These steps must be followed when converting 11-μm radiances between HIRS and AVHRR. Also note that the brightness-temperature adjustment applied in this study applies only to *NOAA-9* data for Wisconsin, in 1986.

This procedure becomes necessary in computing cloud fractional cover using a temperature threshold method and in the computation of cloud emittances for the individual AVHRR pixels. In order to calculate the individual AVHRR pixel 11-μm emittances, both the black-cloud radiance and the clear-sky 11-μm radiance must be known. The clear-sky and black-cloud radiances are derived from HIRS sounding channel analysis. The brightness temperature offset between the HIRS and AVHRR 11-μm channels is used to convert the HIRS 11-μm clear-sky and black-cloud radiances to an equivalent AVHRR 11-μm black-cloud radiance, thus providing the necessary information for the individual AVHRR pixel emittance calculations.

c. Clear-sky albedo map

In order to adjust bidirectional reflectances measured from AVHRR visible channel data for surface reflectance contributions from solar direct and diffuse radiance, knowledge is required of the surface under clear-sky conditions for the same time period. For this study, the measured clear-sky reflectances were derived using the 1.1-km AVHRR channel 1 data during 18 and 19 October 1986, with most of the data coming from October 19. The clear-sky reflectances ρ_{meas} were converted to albedo from

$$\rho_{\text{meas}} = \chi_s(\mu_0, \theta, \phi)\alpha_{\text{clear}}(\Theta, \Phi, \mu_0), \qquad (1)$$

where χ_s is the anisotropic surface reflectance factor with values given by the model of Minnis and Harrison (1984b), α_{clear} is clear-sky albedo, θ is the satellite viewing zenith angle, ϕ is the satellite viewing azimuth angle, Θ is latitude, Φ is longitude, and μ_0 is the cosine of the solar zenith angle θ_0. (A list of symbols is found

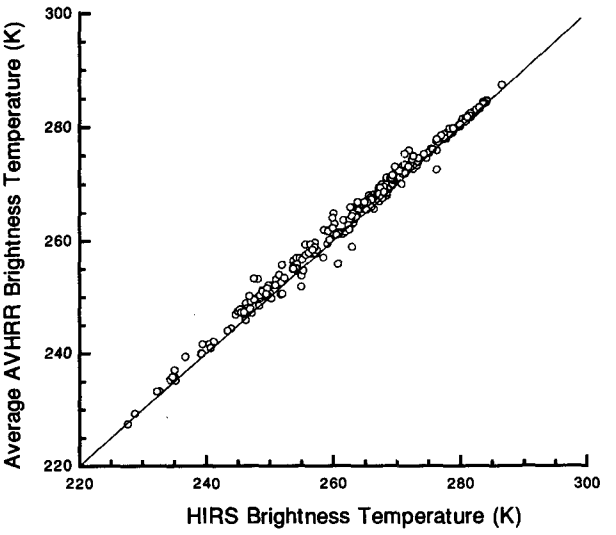

FIG. 3. Comparison of AVHRR and HIRS 11-μm channel brightness temperatures for clear and cloudy conditions on 2 November 1986.

in the Appendix.) The individual clear-sky albedos were averaged to form a $0.1° \times 0.1°$ grid over the IFO mentioned in the previous section. In order to account for the variation of solar zenith angle for any particular satellite overpass, the values of albedo were normalized to a single value of solar zenith angle, 54°, that was representative of solar noon.

d. Rawinsonde data

Rawinsondes were launched from various ground sites during the FIRE mission from locations in Minnesota (St. Cloud, International Falls), Wisconsin (Green Bay, Platteville, Ft. McCoy, Wausau), Michigan (Flint, Sault Ste. Marie), Illinois (Peoria), and Nebraska (Omaha). The sondes provided the temperature and humidity profiles used in this study to generate clear-sky radiance profiles, transmittance profiles, and weighting functions necessary for the analysis of the HIRS and AVHRR data. The temperature and humidity data were used from sondes that were launched within 2 h of the satellite overpass.

4. Determination of cloud properties

a. Clear- and cloudy-sky radiances

The clear-sky spectral radiance $I_{\text{clear}}(\nu, P_{\text{sfc}})$ for a black surface ($\epsilon = 1$) is given by

$$I_{\text{clear}}(\nu, P_{\text{sfc}}) = B(\nu, T_{\text{sfc}})\tau(\nu, P_{\text{sfc}}) + \int_{P_{\text{sfc}}}^{0} B[\nu, T(P)] \frac{d\tau(\nu, P)}{d \ln P} d \ln P, \quad (2)$$

where $B(\nu, T)$ is the Planck radiance at wavenumber ν and temperature T, $\tau(\nu, P)$ is the transmission from atmospheric level P to the satellite at $P = 0$, the subscript "clear" denotes clear-sky conditions, and the subscript "sfc" denotes the surface.

For an overcast FOV, the radiance for a black cloud at pressure level P_{cld} is given by

$$I_{\text{cld}}(\nu, P_{\text{cld}}) = B(\nu, T_{\text{cld}})\tau(\nu, P_{\text{cld}}) + \int_{P_{\text{cld}}}^{0} B[\nu, T(P)] \frac{d\tau(\nu, P)}{d \ln P} d \ln P, \quad (3)$$

where the subscript "cld" denotes cloud. Emittance and transmittance are related by $\epsilon(\nu) + \tau(\nu) = 1$ since it is assumed that reflectance at the thermal infrared wavelengths between 10 and 14 μm is negligible. As a result of this assumption, the fractional coverage A_{cld} for a nonblack cloud with emittance ϵ in an FOV is equivalent to an effective cloud amount of ϵA_{cld} for a black cloud. For a partially cloud-filled FOV, then, we calculate the theoretical upwelling radiance that should be measured by a satellite at a particular wavenumber as

$$I_{\text{calc}}(\nu) = I_{\text{clear}}(\nu) + \epsilon(\nu)A_{\text{cld}}[I_{\text{cld}}(\nu) - I_{\text{clear}}(\nu)]. \quad (4)$$

The transmission functions used in (2) and (3) are calculated using the methods detailed in Weinreb et al. (1981). The calculations take into account both vertical and slant paths, the effect of a varying temperature profile, absorption by well-mixed gases (including nitrogen, oxygen, and carbon dioxide), water vapor (including the water vapor continuum), and ozone. Note that the transmission functions for the HIRS channels are first estimated from theoretical line-by-line calculations of spectral absorption. The transmission functions are then empirically tuned by matching simultaneous HIRS and radiosonde-observed temperature and water vapor profiles (Weinreb et al. 1981). This procedure eliminates any biases in the transmission functions that might be caused by uncertainties in theoretical absorption line parameters or in the HIRS channel spectral response. This procedure will also eliminate biases in cloud pressure derived using HIRS data.

The weighting functions ($d\tau / d \ln P$) are dependent on the temperature and water vapor profiles, but vary only slightly with changes in these profiles. The integrals in (2) and (3) are evaluated by integrating over 40 discrete pressure levels between 1000 and 0.2 mb. The temperature and the logarithm of water vapor mixing ratio are assumed to be linear with the logarithm of pressure.

b. Cloud-pressure retrieval

The rawinsonde profiles from ground stations within the IFO are used to calculate the Planck function and transmission functions required to obtain the clear-sky radiance in (2). From (3), a set of theoretical cloudy-sky radiances are derived that are functions only of cloud-top pressure P_{cld} and scan angle. The change in measured radiance at a particular wavenumber due to the presence of cloud is called the cloud signal. The cloud signal is calculated from (4) and is given by

$$\Delta I^i_{\text{cld}} = I^i_{\text{calc}} - I^i_{\text{clear}} = \epsilon^i A_{\text{cld}}[I^i_{\text{cld}}(P_{\text{cld}}) - I^i_{\text{clear}}], \quad (5)$$

where the superscript denotes channel wavenumber dependence. For N channels chosen, a set of N equations is obtained for $N + 2$ unknowns, namely, A_{cld}, P_{cld}, and N emittances. We assume that emittances for the N channels are equal. This assumption is valid when the channels are spaced closely in wavenumber. Instrument noise is assumed to be Gaussian with a zero mean and a standard deviation of 0.22 mW m^{-2} sr^{-1} cm for the 15-μm channels (Wielicki and Coakley 1981). The cloud signal must be greater than ten times the signal noise for the HIRS pixel to be flagged as registering cloud. In this study, we employ two different techniques for the calculation of cloud pressure and effective cloud amount from (4).

The radiance ratioing method is the first technique considered and uses two channels ($N = 2$) closely

spaced in wavenumber. This method, described more fully in Smith and Platt (1978) and McCleese and Wilson (1976), considers the function given by

$$G^{ij}_{\text{calc}}(P_{\text{cld}}) = \frac{\Delta I^i_{\text{cld}}}{\Delta I^j_{\text{cld}}} = \frac{[I^i_{\text{cld}}(P_{\text{cld}}) - I^i_{\text{clear}}]}{[I^j_{\text{cld}}(P_{\text{cld}}) - I^j_{\text{clear}}]}, \quad (6)$$

where $G^{ij}_{\text{calc}}(P_{\text{cld}})$ is a ratio of the cloud effect in two channels. Since the two channels are spaced closely in wavenumber, the assumption is made that the emittances in the adjacent channels are equal so that from (5), $G^{ij}_{\text{calc}}(P_{\text{cld}})$ can be seen to be independent of ϵA_{cld}. In order to derive the cloud-top pressure in the FOV, the $G^{ij}_{\text{calc}}(P_{\text{cld}})$ ratio calculated using the measured temperature and humidity profiles in (6), (3), and (2) is compared to the G^{ij}_{meas} ratio determined using measured radiances in (7).

The measured G^{ij}_{meas} ratio is given by

$$G^{ij}_{\text{meas}} = \frac{(I^i_{\text{meas}} - I^i_{\text{clear}})}{(I^j_{\text{meas}} - I^j_{\text{clear}})}, \quad (7)$$

where I^i_{meas} and I^j_{meas} are the measured radiances in channels i and j, respectively. The equivalence of (6) and (7) can be seen from (5).

In general, the accuracy with which G^{ij}_{meas} can be measured to determine cloud height is a function of the channel combination used, the cloud height, and the effective cloud amount (Wielicki and Coakley 1981). Sources of error in the measured G^{ij}_{meas} are instrument noise and uncertainty in the clear-sky radiance. Cloud-height retrieval error increases with decreasing cloud height and with decreasing ϵA_{cld} (Wielicki and Coakley 1981). The result simply points out that error increases as cloud signal decreases. An error in cloud-height retrieval may also be expected when multilevel clouds are present and the uppermost layer is not optically thick. In this case, the satellite radiometers will be measuring the radiance from more than one cloud layer, thereby making interpretation of the measured radiance much more difficult. The optimum selection of sounding channels varies with cloud height. If one or both of the sounding channels chosen happen to peak at levels of the atmosphere above the cloud, then (2) and (3) show that $I^i_{\text{cld}} \approx I^i_{\text{clear}}$, a result that provides little cloud information. In general, the peak of both sounding-channel weighting functions should be at or below the cloud height to be retrieved.

The present study uses the HIRS channel combination of 6/7 in the 15-μm CO_2 band. Channel 6 has a weighting function that peaks at about 700 mb, and accordingly has a small transmission at the surface. Channel 7 has a weighting function that peaks at approximately 950 mb. Since this channel has a higher transmissivity at the surface than channel 6, it is more sensitive to variations in surface temperature. Both channels usually provide large signals when cirrus clouds are present.

The second technique used to derive cloud height is based upon the minimization of the root-mean-square (rms) difference between calculated and observed radiances. This method, proposed by Chahine (1974), also assumes a knowledge of temperature and humidity profiles. The rms radiance difference for N channels is determined from

$$I_{\text{rms}}(P_{\text{cld}}, \epsilon A_{\text{cld}}) = \{\sum_{i=1}^{N} [I^i_{\text{meas}} - I^i_{\text{calc}}(P_{\text{cld}}, \epsilon A_{\text{cld}})]^2\}^{1/2}, \quad (8)$$

where I^i_{meas} denotes the measured radiance of channel i and $I^i_{\text{calc}}(P_{\text{cld}}, \epsilon A_{\text{cld}})$ denotes the radiances calculated from (4). The atmosphere between 200 and 950 mb is divided into 25-mb intervals for the rms calculations. Thus, the derived cloud pressure will correspond to the rms minimum at a defined interval.

The value of ϵA_{cld} is calculated using (4) for the lowest sounding channel, which in this case is channel 7. In this case, the difference in (8) will be zero for channel 7 but nonzero for all other channels.

The results of the rms analysis using only HIRS channels 6 and 7 are approximately the same (i.e., within 25 mb) as the ratio method result, as expected. At a minimum, the lowest two sounding channels are used for the rms cloud pressure calculations. If the cloud signal is very strong, HIRS channels 4 and 5 may also be included in the retrieval. Addition of HIRS channels 4 and 5 may not always help in the cloud-pressure retrieval. Channels 4 and 5 have weighting functions that peak at approximately 300 and 500 mb, respectively. If the weighting function of the added sounding channel peaks at or above the cloud, the additional rms noise may prevent a well-defined rms minimum from forming. A well-defined minimum in this study is defined to be a minimum that is at least 20% less than the rms values of adjacent pressure levels. The total number of sounding channels used to calculate cloud pressure for each HIRS pixel thus depends on the additional rms noise.

Comparisons by Wylie and Menzel (1989) of VAS [Visible–Infrared Spin Scan Radiometer (VISSR) Atmospheric Sounder] infrared sounder–derived cloud heights with FIRE lidar data and stereo cloud-height data found that cloud-height error for this technique is about 0.5 to 1.0 km at cirrus altitudes. This result is consistent with earlier theoretical error analyses by Wielicki and Coakley (1981). Note that the HIRS-derived cloud pressure is expected to be near cloud center for optically thin cloud ($\delta_{\text{ext}} < 1$), where δ_{ext} is the extinction optical depth. The cloud pressure is expected to increase to cloud top for more nearly opaque cloud ($\delta_{\text{ext}} > 1$).

The cloud-top pressure derived using the rms method discussed in this section will be used to determine individual AVHRR pixel emittances in section 5c.

c. HIRS pixel cloud fraction

One of the common assumptions made with many cloud-retrieval algorithms is that the FOV is either completely cloud filled or completely clear. That is, cloud cover is either 0 or 1 for each pixel. The determination of whether a pixel is cloud filled or could be arrived at, for example, by using either a visible-channel reflectance threshold or an 11-μm channel brightness temperature threshold. This assumption does not take subpixel-scale cloudiness into account. The assumption that the pixel is either cloud filled or completely clear is less accurate for the 18-km HIRS pixel than for the 1.1-km AVHRR pixel.

Some algorithms try to account for fractional cloudiness, however. The spatial coherence technique of Coakley and Bretherton (1982) accounts for partial cloud cover explicitly in AVHRR 4-km pixels containing optically thick cloud in a single cloud layer. The hybrid bispectral threshold method (HBTM) (Minnis and Harrison 1984a) accounts for partial cloud cover implicitly through application of reflectance and 11-μm brightness-temperature thresholds to histograms of a scene. The maximum-clustering technique of Arking and Childs (1985) also attempts to account for partial cloud cover. The clustering technique requires that the cloud have a uniform optical thickness over a region of approximately 0.6° × 0.6°. Unfortunately, inspection of lidar observations (e.g., Spinhirne et al. 1988; Spinhirne and Hart 1990; Sassen et al. 1990; Grund and Eloranta 1990) shows that assumptions of optically thick cloud or uniform optical thickness are difficult to justify for cirrus clouds.

Most of the work presented in the literature to date has addressed the problem of cloud fraction with boundary-layer clouds. Recent studies of the errors in threshold-derived cloud cover using Landsat data (Wielicki and Welch 1986; Parker and Wielicki 1990) concluded that while subpixel-scale cloudiness caused significant errors at 1-km resolution for boundary-layer clouds (i.e., cumulus and stratocumulus), very small errors (0.01) were found for cirrus. These studies did not extend the pixel resolution to the size of the HIRS FOV, however.

Since high-resolution 1.1-km AVHRR pixels are collocated with each HIRS FOV, the fractional cloud cover A_{cld} in each HIRS FOV can be determined by applying a threshold technique to the AVHRR data. The threshold technique may use either an IR channel or a visible channel. The IR threshold technique first uses rawinsonde data to calculate a clear-sky brightness temperature T_{clr}^{BB}. This brightness temperature varies slightly with scan angle, and calculated T_{clr}^{BB} values are stored in lookup tables. Each AVHRR pixel is compared individually against T_{clr}^{BB}. If the measured T_{clr}^{BB} is greater than the calculated T_{clr}^{BB} at a certain scan angle, then the calculated brightness temperature is updated for that particular scan angle in the lookup table and for scan angles within 2° of that point. Following the approach used in the ISCCP (Rossow et al. 1988), the thresholds are set to $T_{clr}^{BB} - 6$ K over land and $T_{clr}^{BB} - 3$ K over water. The presence of cirrus shows up more strongly in the infrared than the visible and has the added benefit of being useful for both daytime and nighttime retrievals. For these reasons, only the brightness temperature threshold is used in this analysis.

5. Results

a. HIRS subgrid-scale cloud fraction

The merged AVHRR–HIRS data for 2 November 1986 at 2001 UTC are used to examine the distribution of cloud cover in HIRS pixels for the 5° × 5° region defined in section 3. This date was an ideal day for observing cirrus, and an 11-μm image of this scene is shown in Fig. 4. The results of using an infrared brightness-temperature threshold are shown in Fig. 5 for 2 November 1986. The histogram shows only the HIRS pixels flagged as having a nonzero effective cloud amount. For this particular scene, approximately 60% of the HIRS pixels are completely filled with cloud, with the remaining pixels partially filled with cloud. The distribution shown depends to some degree on the brightness-temperature threshold chosen, but changing the threshold does not change the overall result that a large fraction of HIRS pixels has subgrid-scale cloudiness. HIRS sounding-channel analysis alone can be used to provide cirrus cloud height and emittance information by assuming that the cloud fraction is 1. However, our results show that it may be more appropriate to use HIRS only to determine cloud height and then use the higher-resolution AVHRR data to determine cloud fraction and cloud emittance for the case of cirrus.

b. Consistency of retrieved cloud pressure

Two techniques were mentioned earlier that made use of the HIRS 15-μm sounding channels, namely, the ratio method and the rms method. An important consideration in the cloud retrieval is the measure of consistency between the two techniques. Note that the rms method calculates cloud pressure by determining the rms minimum at 25-mb intervals. The ratio method calculates cloud pressure by matching the ratio of measured cloud signal in two HIRS channels (G_{meas}^{ij}) to the theoretical $G_{calc}^{ij}(P_{cld})$ profile as calculated in (6). The cloud pressure in this case is derived through interpolation of G_{meas}^{ij} in the $G_{calc}^{ij}(P_{cld})$ profile and is not limited to 25-mb intervals as with the rms method.

In Fig. 6, the retrieved cloud pressure from the ratio method (channels 6/7) is compared to the retrieved cloud pressure using the rms method for 28 October

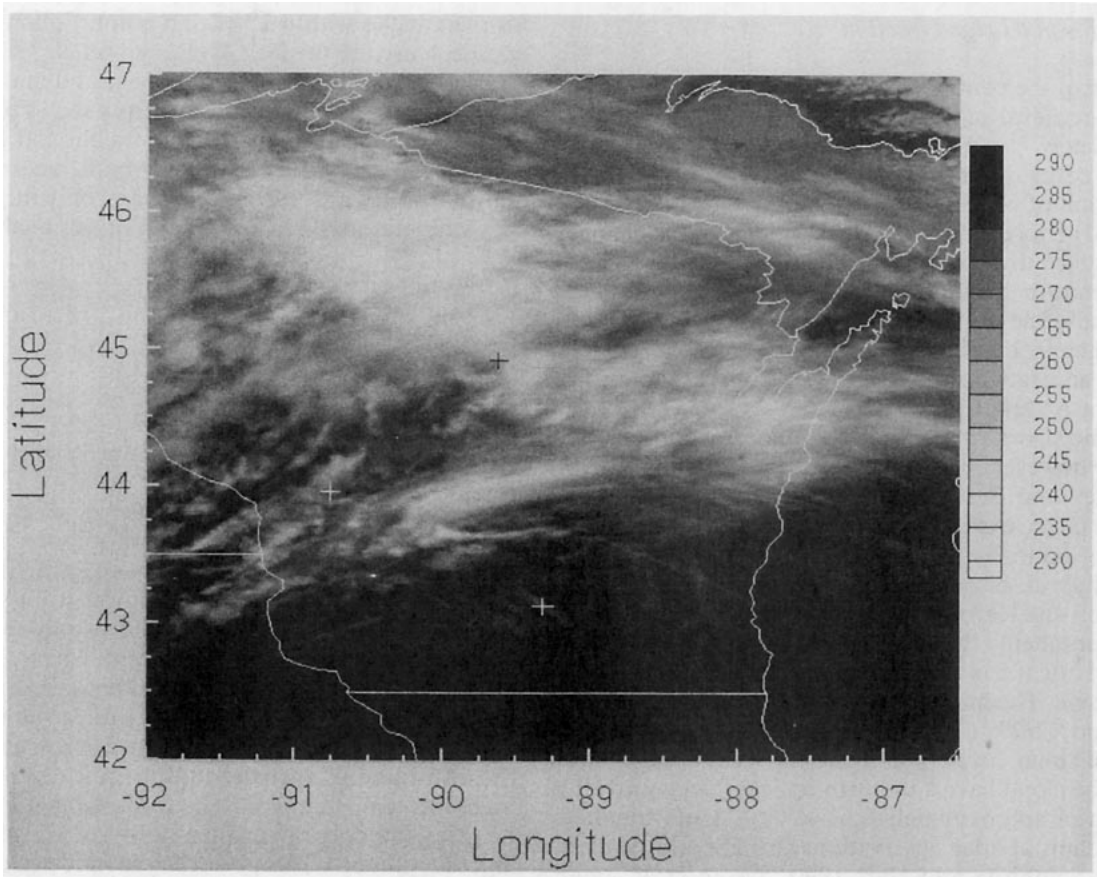

FIG. 4. AVHRR 11-μm image of 2 November 1986, showing the presence of cirrus over the FIRE region. The "+" symbols denote the surface lidar sites described in the text.

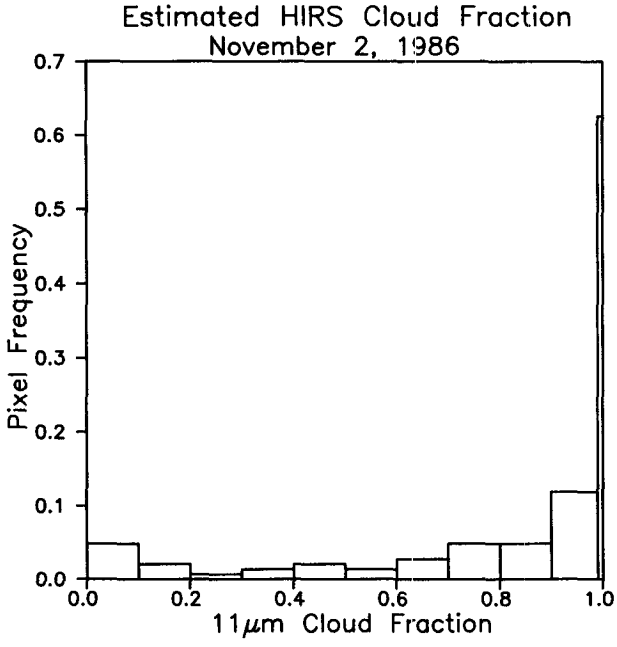

FIG. 5. AVHRR-derived cloud fraction for HIRS pixels on 2 November 1986.

1986. The mean and standard deviation of the difference between the cloud pressures derived from the ratio method and the rms method is −2 and 30 mb, respectively. Similar results are presented in Fig. 7 for 2 November 1986. The mean and standard deviation of the difference between the cloud pressures derived from the ratio and rms method are −6 and 31 mb, respectively.

The HIRS algorithm provides a cloud-top pressure for optically thick cloud (where $\delta_{ext} \gg 1$) but a cloud-radiometric-center pressure for optically thin cloud such as cirrus. One way to determine the accuracy of the retrieved cloud pressure is to compare the algorithm results with either ground-based or aircraft-based lidar profiles. As part of the FIRE mission, several ground-based lidar sites were employed in Wisconsin. The lidars deployed at Madison and Wausau have the ability to determine cloud thickness up to an optical depth of about 1, while the lidar at Fort McCoy has the ability to determine cloud thickness up to an optical depth of about 3.

There is no direct way to compare the cloud heights determined from a very thin lidar beam to the cloud heights derived from HIRS–AVHRR satellite radi-

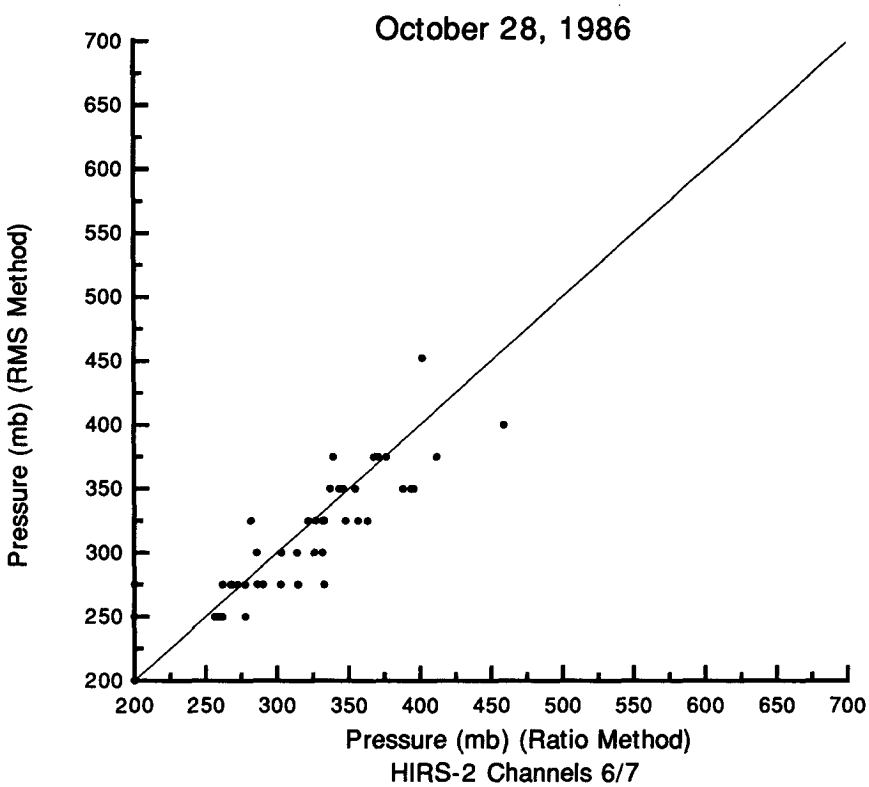

FIG. 6. Comparison of ratio method versus rms method for HIRS derived cloud pressure on 28 October 1986.

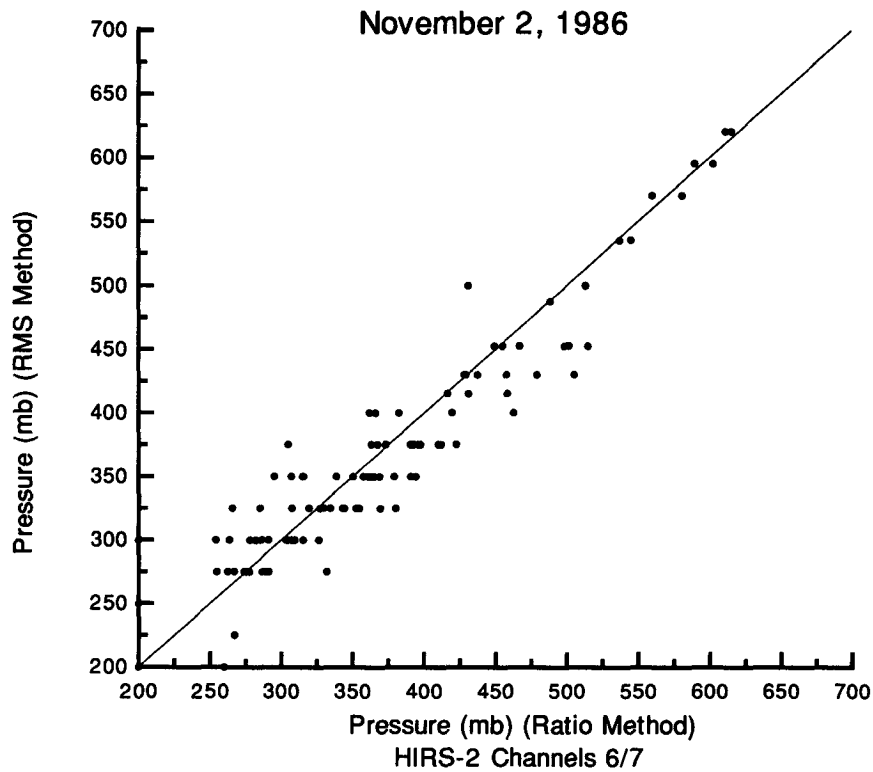

FIG. 7. Comparison of ratio method versus rms method for HIRS derived cloud pressure on 2 November 1986.

TABLE 2. Comparison of HIRS retrieved cloud heights, using the rms method and using an assumption of black cloud at 11 μm, to lidar cloud heights. Cloud height Z is derived using (a) the rms method, (b) lidar, in which case the cloud-base height (bot), cloud-center height (ctr), and cloud-top height (top) is given, or (c) the 11-μm channel with a black-cloud assumption. Standard deviations of cloud height are given by σ. The lidar stations represented are Wausau (WAU), Fort McCoy (FTM), Madison (MAD), or the NASA ER-2 aircraft (ER-2).

Station	Julian day	Z^{rms} (km)	σ^{rms} (km)	Z^{lidar}_{bot} (km)	Z^{lidar}_{ctr} (km)	Z^{lidar}_{top} (km)	$Z^{11\,\mu m}$ (km)	$\sigma^{11\,\mu m}$ (km)
WAU	306	7.9	0.5	5.0	5.6	8.4	6.2	1.2
FTM	306	8.6	2.5	7.0	8.4	9.7	3.3	0.9
WAU	301	9.2	1.9	7.4	8.5	10.5	3.7	1.1
FTM	301	10.5	0.1	8.3	8.8	10.5	5.0	1.9
MAD	301	10.2	0.6	8.1	9.8	10.5	5.3	2.0
ER-2	306	7.9	0.6		8.2		5.8	1.0

ometry unless the HIRS FOV includes the lidar site. In the discussion of Fig. 1, it was shown that there is a gap between consecutive HIRS pixels both along a scan line and between scan lines. Therefore, there is no guarantee that any particular HIRS pixel will cover a lidar site completely. A lidar site may indeed fall near the edge of a HIRS pixel, between consecutive pixels, or in the gap between scan lines.

With this caveat, a comparison of HIRS-derived cloud heights using the ratio method with lidar results is presented in Table 2 and shown in Fig. 8. The data are taken from 1939 UTC 27 October 1986, 2055 UTC 28 October 1986, and 2005 UTC 2 November 1986, as reported in Minnis et al. (1990). For each surface lidar site, the cloud heights from the four closest HIRS pixels are averaged to provide a mean and standard deviation height that is subsequently compared to lidar data. The stations in the table represent ground-based lidar locations at Wausau (WAU), Fort McCoy (FTM), and Madison (MAD). The ER-2 lidar data were handled differently. For this one case, eight HIRS pixels straddling the flight overpath were averaged. All the ER-2 lidar data were averaged from 1159 to 2012 UTC to derive a mean cloud height of 8.2 km and a standard deviation of 0.7 km. In the table, the mean HIRS cloud heights derived from using the rms method are presented in column 3 and the standard deviations are in column 4. Columns 5, 6, and 7 show the lidar cloud-base height, lidar cloud-center height, and lidar cloud-top height. For comparison, the cloud heights and their standard deviations that would be derived using an assumption of black cloud (i.e., $\epsilon = 1$) in each HIRS pixel is given in the final two columns in the table. As expected, the black-cloud assumption tends to greatly underestimate cloud height when the cloud emittance is less than 1.

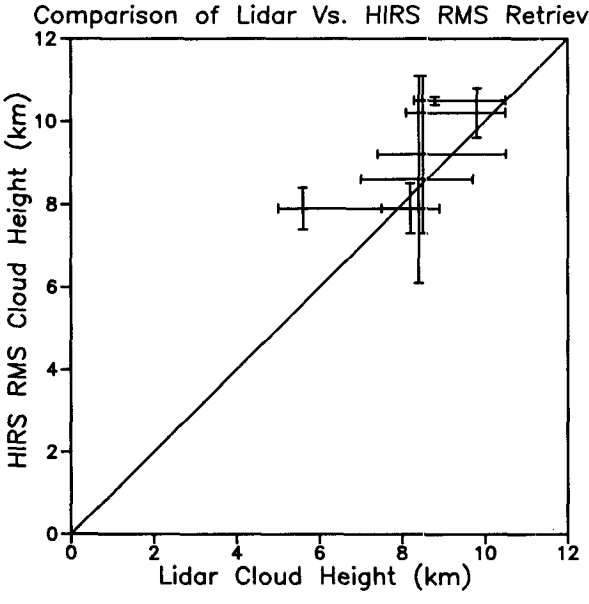

FIG. 8. Comparison of HIRS rms method retrieved cloud height versus lidar cloud height.

The comparison of the HIRS cloud heights derived from the rms method to the lidar cloud heights are plotted in Fig. 8. The vertical error bars show the standard deviation in height of the four HIRS pixels. The horizontal error bars show the cloud thickness estimated from the lidar data. The results show that these two error sources inherent in comparing satellite-retrieved cloud heights to ground-based lidar greatly complicate comparisons to cloud "truth." It is possible that the retrieved cloud heights may be higher than surface-based lidar heights for optically thick clouds. The reason is that the lidar signal may be completely attenuated by the time the cloud optical thickness is greater than approximately 3, while the satellite is viewing the same cloud from above. At present, there are too few points to determine whether there is a consistent bias present in the HIRS cloud retrieval algorithm.

The problem of determining a radiatively effective cloud height at 11 μm using lidar data has been addressed by Spinhirne and Hart (1990). This radiatively effective cloud height was used for the ER-2 lidar data in Fig. 8 (Spinhirne 1990, personal communication) but is unavailable for the surface lidar data, which lacked uplooking 11-μm radiometers. The ER-2 and HIRS mean cloud heights agreed within 0.3 km for the case of 2 November 1986.

c. Reflectance–emittance calculations

The primary advantage of the HIRS cloud-height retrieval is to provide an improved estimate of cloud height for optically thin high cloud. The present study will use this capability to examine the relationship of cirrus visible reflectance determined from AVHRR channel 1 radiometric data to thermal infrared emittances derived from AVHRR channel 4 radiometric data. This relationship is used by ISCCP to avoid the assumption of optically thick clouds in the thermal infrared.

For each AVHRR pixel within a HIRS pixel, the cloud-emission radiance $I_{cld}(P_{cld})$ derived using the HIRS sounding channel rms method is used with the AVHRR channel 4 measured radiance to derive an estimate of cloud emittance at 11 μm. The viewing zenith-angle–dependent emittance can be derived from (4), after substituting $I_{calc}(P_{cld})$ with I_{meas}, to obtain

$$\epsilon(\theta) = \frac{(I_{meas} - I_{clear})}{[I_{cld}(P_{cld}) - I_{clear}]}, \quad (9)$$

where I_{meas} is the measured radiance. The vertical emittance can be calculated as in Platt et al. (1980), that is, by first defining the IR optical depth at the viewing zenith angle θ,

$$\delta_{abs}(\theta) = -\ln[1 - \epsilon(\theta)]. \quad (10)$$

The vertical emittance is then given by

$$\epsilon_v = 1 - \exp[-\delta_{abs}(\theta)\cos(\theta)]. \quad (11)$$

Reflectance for each AVHRR pixel is determined as a bidirectional reflectance ρ_{meas}:

$$\rho_{meas} = \frac{\pi I}{S\mu_0}, \quad (12)$$

where I is the shortwave spectral radiance in AVHRR channel 1, S is the incoming solar spectral flux for channel 1, and μ_0 is the cosine of the solar zenith angle. As discussed earlier, conversion of counts to radiance for the solar channels is taken from Whitlock et al. (1990).

The cirrus clouds under study are generally semitransparent, so the cloud signal from the visible channels is contaminated with both direct and diffuse solar radiation that has been transmitted through the cloud and reflected by the surface. A surface reflectance correction is necessary to compare measured reflectances directly to radiative transfer calculations that use a black-surface assumption. The procedure used to subtract the surface-reflected direct and diffuse solar radiation components from the AVHRR measured reflectances is that given by Minnis et al. (1990):

$$\rho_{meas} = \tau_a\rho_{cld} + \rho_{g1}\tau_d\tau_u + \alpha_{g2}(1 - \bar{\alpha}_{cld})(1 - \tau_u - \alpha_{cld}), \quad (13)$$

where ρ_{meas} is the measured bidirectional reflectance using (12), ρ_{cld} is the cloud bidirectional reflectance, α_{cld} is the cloud albedo at solar zenith angle θ_0, ρ_{g1} is the surface bidirectional reflectance, α_{g2} is the albedo of the surface to diffuse incoming radiation (from the cloud), $\bar{\alpha}_{cld}$ is the cloud diffuse albedo, τ_a is the transmittance above the cloud, τ_d is the transmission of direct solar radiation through the cloud to the surface, and τ_u is the transmittance of direct solar radiation between the surface and the satellite. The cloud reflectance ρ_{cld} is equal to $\alpha_{cld}\chi(\theta_0, \theta, \phi)$, the product of the cloud planar albedo and the cloud anisotropic factor. No simple parameterization exists as yet for the cloud anisotropic factor. The first term on the right accounts for solar radiation scattered from the cloud to the satellite. The second term in (13) accounts for direct solar radiation transmitted through the cloud that reflects from the surface toward the satellite. The third term in (13) represents a source of diffuse radiation transmitted through the cloud, reflected from the surface, and transmitted through the cloud in the path of the satellite sensor. The transmittance τ_a of the air above the cloud accounts for ozone absorption and is derived using a parameterization from Rossow et al. (1988),

$$\tau_a = \exp\left[-u(0.085 - 0.00052u)\left(\frac{1}{\mu_0} + \frac{1}{\mu}\right)\right], \quad (14)$$

where u is the ozone abundance (cm STP), μ_0 is the cosine of the solar zenith angle, and μ is the cosine of the viewing zenith angle. The value of u used in this study, 0.32, is an average of the values assumed for midlatitude winter and summer standard atmospheres above 10 km from McClatchey et al. (1973) and is the same as that used in Minnis et al. (1990). Note that τ_a is included implicitly in the second and third terms of (13) through the use of a measured value of ρ_{g1}. The transmittance of the cloud due to direct solar radiation for a visible optical depth δ_{ext} is given by Platt et al. (1980) as

$$\tau_d = \exp(-\delta_{ext}/2\mu_0). \quad (15)$$

However, the transmittance of direct solar radiation between the surface and the satellite depends on the viewing zenith angle

$$\tau_u = \exp(-\delta_{ext}/2\mu). \quad (16)$$

The factor of 2 is included since the particle size is assumed to be much greater than the wavelength. In this case, half of the scattered radiation is assumed to be diffracted close to the forward direction and can be considered as unscattered (Platt et al. 1980; Takano and Liou 1989a). The reflected diffuse albedo α_{g2} may be computed from the surface reflectance ρ_{g1} through use of the ERBE angular shortwave radiation models (Suttles et al. 1988), using either clear land or clear ocean as the reflective surface. The surface reflectance is known through the use of the clear-sky albedo map, using the appropriate viewing conditions and the bidirectional reflectance model previously described. The

cloud diffuse albedo, $\bar{\alpha}_{cld}$, is calculated using a delta-Eddington code to derive planar albedo for different optical depths at varying solar zenith angles.

For the reflectance–emittance analyses presented in the next section, the HIRS cloud-pressure retrieval uses the results from the rms method, since this method should give better results for high cloud (Wielicki and Coakley 1981). Results interpolated from lookup tables based on theoretical calculations (Minnis 1991) are shown in Figs. 9–13. Four scattering phase functions were used for the theoretical calculations, a Mie phase function for spherical water droplets with equivalent radius of 10 μm (Rossow et al. 1988) and three phase functions representing randomly oriented hexagonal ice crystals of varying size distributions as in Takano and Liou (1989a). One ice-crystal-size distribution represents cirrostratus (Cs), and another size distribution represents cirrus uncinus (Cu), both presented by Heymsfield (1975). The equivalent aspect ratios $L/2a$ for the Cs and Cu distributions are 35/30 and 115/58, respectively, where L and a represent the length and radius of the hexagonal ice crystal.

The lookup tables (Minnis 1991) were generated using the adding–doubling method for a single scattering layer as described in Takano and Liou (1989b) at wavelengths of 0.55 and 10.8 μm. Results from theoretical calculations using theoretical phase functions at 10.8 μm for the same particle distributions were used to account for scattering in the thermal infrared (Minnis 1991). The calculation using the Mie phase function is equivalent to the assumption made by ISCCP that the ratio of 0.55-μm scattering optical depth to 11-μm absorption optical depth, denoted by γ, is 2. Effective emittance at 10.8 μm from theory is calculated as for the satellite data in (9).

The conditions at 2005 UTC 2 November 1986 were nearly ideal for viewing thin cirrus cloud since there were regions that clearly had only one type of cloud present. At 1930 UTC 27 October 1986, a band of cirrus was present over the western portion of the IFO, but the satellite was viewing the cloud from a very high viewing zenith angle. Since the HIRS FOVs that fell over the cloud were at the edge of the scan line, the HIRS pixels were large in size and few in number. The situation on 28 October 1986 at 2055 UTC was also complicated, since a front was moving through Wisconsin and multilayer cloud decks were observed during the satellite overpasses. Multilayer cloud decks greatly increase the complexity and error associated with cloud-retrieval algorithms. For these reasons, the reflectance–emittance discussion begins with the less complex case of 2 November 1986.

d. Reflectance–emittance results

1) 2 NOVEMBER 1986

Three sets of HIRS–AVHRR data for 2 November 1986 are shown, each with a different viewing zenith angle. The first example of the reflectance–emittance relationship is taken from HIRS pixels located over Lake Michigan. In this case, the solar zenith angle is 68°, the viewing zenith angle is 5°, and the azimuthal angle is about 36°. Forward scattering corresponds to 0°, and backward scattering corresponds to 180°. The scattering phase angle, defined as the angle between the incoming light and the outgoing scattered light, is approximately 110°. The magnitude of the surface reflectance correction for AVHRR pixels over Lake Michigan is about 0.04 for very thin cirrus, decreasing to zero for optically thick cirrus. The correction causes observed reflectances to tend to zero as cirrus optical depth decreases. Figure 9 plots reflectance against emittance using the AVHRR pixels collocated with five HIRS pixels centered over Lake Michigan, southwest of Green Bay. This area has a thin layer of cirrus overlying the lake. Analysis of these HIRS pixels shows that over Lake Michigan, the cirrus is not uniform in height or emittance. Table 3 gives the HIRS–AVHRR-derived cloud properties in each pixel. The second column in the table and each subsequent table presents a symbol associated with each HIRS pixel. These symbols are used in the reflectance–emittance figures discussed later in the text. The table shows the latitude and longitude of each HIRS pixel, the cloud pressures derived from the ratio method (channels 6/7) and the rms method, and the average vertical emittance and average reflectance derived from the AVHRR pixels collocated with

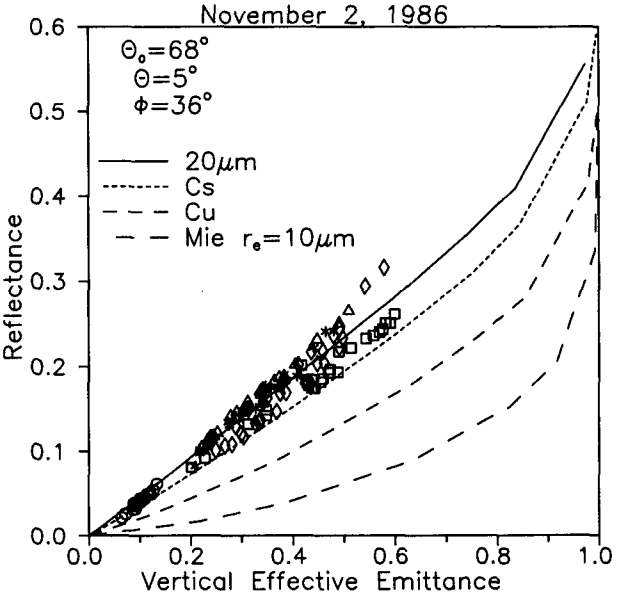

FIG. 9. Comparison of AVHRR–HIRS-derived cloud bidirectional reflectances at 0.63-μm and 11-μm vertical effective emittance with theoretical computations of reflectances at 0.55 μm and emittances at 10.8 μm for various cloud-particle distributions as described in the text. The symbols used in the figure are explained in the text. The data are taken from 2 November 1986 for θ_0 = 68°, θ = 5°, ϕ = 36°.

TABLE 3. Cloud characteristics at 2005 UTC 2 November 1986 for the following viewing conditions: $\theta_0 = 68°$, $\theta = 5°$, and $\phi = 36°$. The quantities P_{cld} and Z_{cld} refer to cloud pressure, and cloud height, respectively. The quantities ϵ_v^{avg} and ρ^{avg} are the average vertical emittance and average reflectance derived from the AVHRR pixels collocated with each HIRS pixel. The superscripts 6/7, rms, and ISCCP denote quantities derived using the ratio method (using HIRS channels 6 and 7), the rms method, or the ISCCP method, respectively.

HIRS pixel	Symbol	Latitude (°N)	Longitude (°W)	$P_{cld}^{6/7}$ (mb)	$Z_{cld}^{6/7}$ (km)	P_{cld}^{rms} (mb)	Z_{cld}^{rms} (km)	ϵ_v^{avg}	ρ^{avg}	Z_{cld}^{ISCCP} (km)
1	○	43.85	87.0	275	9.7	275	9.7	0.10	0.04	0.6
2	□	44.22	87.1	412	6.9	375	7.6	0.47	0.20	3.1
3	△	44.28	86.8	289	9.4	275	9.7	0.33	0.17	2.8
4	◇	44.65	86.9	200	11.7	250	10.3	0.39	0.18	4.1
5	*	44.71	86.6	200	11.7	250	10.3	0.33	0.16	3.2

each HIRS pixel. The final column shows the cloud height derived using the ISCCP approach and will be discussed further later in this section.

In Fig. 9 and subsequent reflectance–emittance figures, the AVHRR pixels collocated with a HIRS pixel are represented by a symbol as detailed in the second column of the table. Figure 9 shows that for a given 11-μm emittance, reflectances are much larger than predicted by theory for the 10-μm water-sphere calculation but fall within the range of the hexagonal ice-crystal curves. The pixel distribution lies between the cirrostratus and 20-μm ice-particle curves.

The data also indicate that for this viewing geometry, the assumption of spherical water particles could cause an underestimate in cloud height as derived by ISCCP if the clouds are composed of ice crystals. In order to quantify the possible underestimate in cloud heights, cloud heights are calculated using the ISCCP approach and presented in the last column of Table 3. The ISCCP cloud heights are derived in the following way. The average reflectance for a HIRS FOV is calculated from the collocated AVHRR pixels. The corresponding vertical emittance at 11 μm is determined using Fig. 9 for the Mie spherical-water-droplet calculations. The vertical emittance is then converted to the viewing zenith-angle–dependent emittance using (10) and (11). The 11-μm black-cloud radiance $I_{cld}(P_{cld})$ is then calculated from (9). The cloud pressure is determined from the theoretical radiance profiles generated from the rawinsonde temperature and humidity profiles at the appropriate HIRS FOV and scan angle. Finally, cloud height is calculated from the cloud pressure.

The ISCCP cloud heights shown in the table are systematically lower than the HIRS rms cloud heights. The largest discrepancies occur for the HIRS pixels that have a low vertical emittance. These differences are consistent with the theoretical results of Minnis (1991), which showed that cloud heights derived with the ISCCP approach will be underestimated by the greatest amount for thin, high, ice-crystal clouds. Furthermore, the derived optical depth or cloud height is most sensitive to small errors in clear-sky reflectance for very thin clouds. Thus, the uncertainty in the emittance derived from the AVHRR data is greatest for thin clouds.

The next two cases are taken from HIRS pixels located as close to the ER-2 flight path as possible. The viewing conditions are $\theta_0 = 68°$, $\theta = 15°$, and $\phi = 36°$. The scattering phase angle for this case is approximately 100°. The chosen HIRS pixels are detailed in Table 4.

The HIRS-retrieved cloud heights using the rms method have a mean height of 8.4 km and a standard deviation of 0.45 km. The radiatively effective lidar heights reported by Spinhirne (1990, personal communication) provided evidence for radiative cloud heights between approximately 8 and 9 km. The reflectance–emittance relationship for the collocated AVHRR pixels is shown in Fig. 10. As with the first case, the reflectances are higher for any given emittance than would be expected using a Mie water-droplet phase function. However, at high emittances, it seems that the AVHRR pixel reflectances are higher than those predicted by theory, assuming the composition of these clouds is hexagonal ice crystals.

TABLE 4. Cloud characteristics at 2005 UTC 2 November 1986 for the following viewing conditions: $\theta_0 = 68°$, $\theta = 15°$, and $\psi = 36°$. The quantities P_{cld} and Z_{cld} refer to cloud pressure and cloud height, respectively. The quantities ϵ_v^{avg} and ρ^{avg} are the average vertical emittance and average reflectance derived from the AVHRR pixels collocated with each HIRS pixel. The superscripts 6/7, rms, and ISCCP denote quantities derived using the ratio method (using HIRS channels 6 and 7), the rms method, or the ISCCP method, respectively.

HIRS pixel	Symbol	Latitude (°N)	Longitude (°W)	$P_{cld}^{6/7}$ (mb)	$Z_{cld}^{6/7}$ (km)	P_{cld}^{rms} (mb)	Z_{cld}^{rms} (km)	ϵ_v^{avg}	ρ^{avg}	Z_{cld}^{ISCCP} (km)
1	○	44.91	89.6	307	9.0	350	8.1	0.73	0.42	6.9
2	□	44.98	89.3	316	8.8	350	8.1	0.70	0.31	6.0
3	△	45.27	89.8	365	7.8	350	8.1	0.96	0.52	7.9
4	◇	45.35	89.4	343	8.3	325	8.6	0.84	0.41	7.3
5	*	45.42	89.1	278	9.6	300	9.1	0.68	0.30	6.7

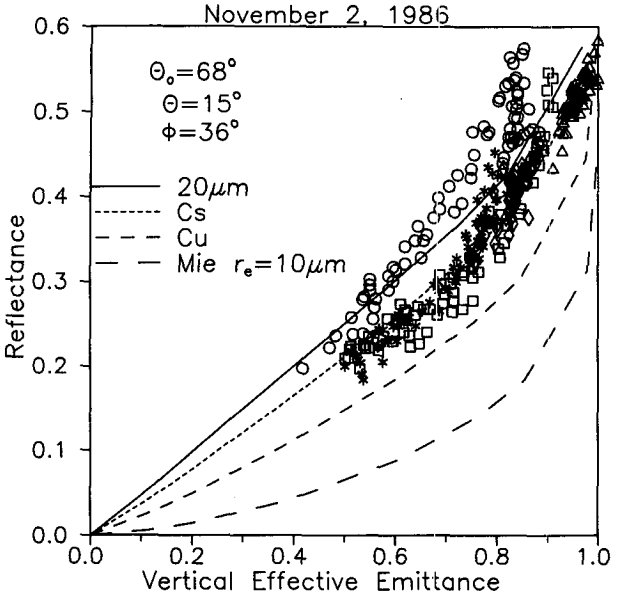

FIG. 10. Same as Fig. 8, except the viewing conditions are $\theta_0 = 68°$, $\theta = 15°$, $\phi = 36°$.

A comparison of the HIRS rms cloud heights with the cloud heights derived using the ISCCP approach shows that, for this case, the cloud heights differ by 2%–26%. The reason the rms and ISCCP cloud heights are closer than the results in the previous case is that the vertical emittances are higher. In the limit of optically thick clouds, the ISCCP and HIRS methods are expected to agree closely.

The third case is for the same solar zenith and azimuthal angles as before, but with a higher viewing zenith angle of 21°. The scattering phase angle is approximately 90°. The HIRS pixels chosen also coincide as closely as possible to the ER-2 flight during this time period. The retrieved cloud characteristics are presented in Table 5.

The retrieved cloud heights have a mean height of 7.5 km using the ratio method results and a standard deviation of 0.4 km. The lidar heights from Spinhirne (1990, personal communication) indicate that cloud heights were generally between 7 and 9 km. The AVHRR pixels shown in Fig. 11 are well above the Mie water-droplet curve for 10-μm droplets, indicating that the clouds contain a distribution of ice crystals with characteristics between the 20-μm crystal and cirrostratus. The results from this choice of HIRS–AVHRR pixels show a slightly different behavior than the previous results. Instead of a rather tight distribution of AVHRR pixels, the results here tend to be more highly scattered, indicating variability of either cloud height or cloud particle shape and size within the HIRS footprint.

The ISCCP-derived cloud heights for this case are lower than the rms cloud heights by 12%–30%. As seen in the 2 November case, the largest differences occur for the HIRS pixels having the lowest emittances.

2) 27 OCTOBER 1986

At 1930 UTC, a band of cirrus is present between approximately 43°–47°N and 91°–92°W. The cirrus does not fall over any of the ground stations, so no surface-based lidar comparisons are possible. Comparisons are made with the ER-2 lidar results (Spinhirne et al. 1988) since the aircraft was in operation at this time. The viewing conditions for this case are $\theta_0 = 60°$; $\theta = 57°$; and $\phi = 38°$, resulting in scattering phase angle of approximately 70°, a condition that is closer to forward scattering than the other cases. The viewing zenith angle indicates that the HIRS pixels used in this analysis come near the end of the scan line, so that the size of the HIRS FOV is approximately 30 km × 60 km. The location of the pixels and the retrieved cloud characteristics are presented in Table 6.

The rms cloud retrieval results give a mean height and standard deviation of 11.5 km and 0.6 km, respectively. The reflectance–emittance relationship for the collocated AVHRR pixels is shown in Fig. 12. The distribution of the data is above the theoretical curves. The retrieved cloud heights indicate that the cloudy pixels are at or near the tropopause. The ER-2 lidar results (Spinhirne et al. 1988) indicate that the cloud was between 8 and 10 km. Further inspection of the HIRS sounding channel data indicated that, compared to the other days, the cloud signal was relatively weak in each channel but was large enough (greater than ten times the signal noise limit defined previously) to reg-

TABLE 5. Cloud characteristics at 2005 UTC 2 November 1986 for the following viewing conditions: $\theta_0 = 68°$, $\theta = 21°$, and $\phi = 36°$. The quantities P_{cld} and Z_{cld} refer to cloud pressure and cloud height, respectively. The quantities ϵ_v^{avg} and ρ^{avg} are the average vertical emittance and average reflectance derived from the AVHRR pixels collocated with each HIRS pixel. The superscripts 6/7, rms, and ISCCP denote quantities derived using the ratio method (using HIRS channels 6 and 7), the rms method, or the ISCCP method, respectively.

HIRS pixel	Symbol	Latitude (°N)	Longitude (°W)	$P_{cld}^{6/7}$ (mb)	$Z_{cld}^{6/7}$ (km)	P_{cld}^{rms} (mb)	Z_{cld}^{rms} (km)	ϵ_v^{avg}	ρ^{avg}	Z_{cld}^{ISCCP} (km)
1	○	44.68	90.7	390	7.4	350	8.1	0.61	0.44	5.5
2	□	44.76	90.4	419	6.9	400	7.2	0.63	0.33	5.0
3	△	44.84	90.0	382	7.5	400	7.2	0.66	0.36	5.4
4	◇	45.04	90.9	390	7.4	375	7.6	0.54	0.28	5.3
5	*	45.12	90.5	410	7.0	375	7.6	0.78	0.47	6.7

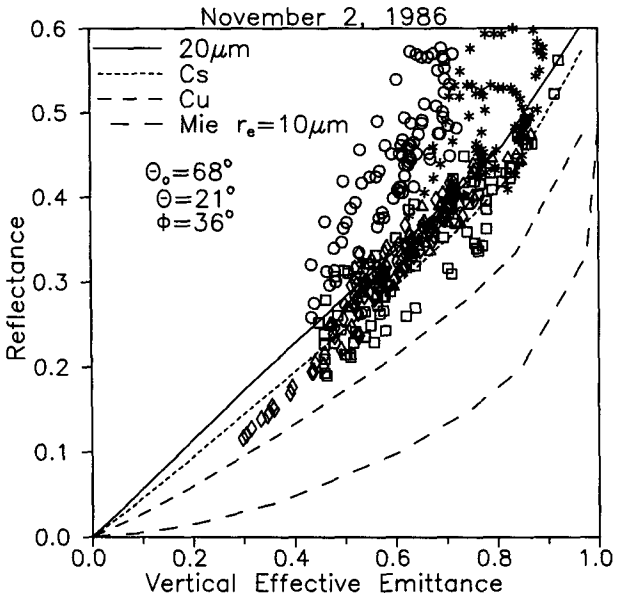

FIG. 11. Same as Fig. 8, except the viewing conditions are $\theta_0 = 68°$, $\theta = 21°$, $\phi = 36°$.

ister cloud as being present. For the ratio method, the cloud signal was approximately the same in both channels, resulting in a high $G^{67}_{\text{meas}}(P_{\text{cld}})$ value that was outside the range of the theoretical $G^{67}_{\text{calc}}(P_{\text{cld}})$ profile. The resulting derived cloud height was at the tropopause for the HIRS pixels in this case. The effect of lowering the clouds is to increase the vertical effective emittance, thereby causing the data to agree better with the theoretical curves.

The vertical emittances for the HIRS pixels in the table are below 0.3, and subsequently the differences between cloud heights calculated from the rms method and the ISCCP algorithm are large.

3) 28 OCTOBER 1986

Similar calculations are performed on 28 October 1986, also for a case over land. As with previous calculations, the surface reflectance is taken into account when correcting for the reflected direct and diffuse solar radiation. Care was taken when choosing HIRS pixels for analysis so that the background reflectance over a small region was as close as possible to being homogeneous, meaning that the surface area did not have large lakes, rivers, or much change in ground cover. HIRS pixels were chosen from the vicinity of Wausau and are listed in Table 7 with the retrieved cloud characteristics. Cloud heights ranged from 6.4 to 10.5 km. The viewing conditions given in Table 7 yield a scattering phase angle of approximately 140°. For this case, the magnitude of the reflectance correction ranges from about 0.1 to 0.15 for very thin cirrus, decreasing to zero for optically thick cloud. The meteorological situation on 28 October is more complicated, with a wide variety of clouds over Wisconsin (Starr and Wylie 1990).

The cloud-height retrievals using the rms method have a mean height and standard deviation of 9.4 and 1.7 km, respectively. The resulting reflectance–emittance relationship (Fig. 13) shows that the distribution of AVHRR pixels again falls above the Mie curve and the ice-crystal curves. The increased scatter implies varying cloud height and ice-particle size or shape, consistent with other analyses of the cirrus on 28 October 1986 (Wielicki et al. 1990). The distribution of points above the theoretical curves could be the result, for example, of having smaller ice crystals or of nonhexagonal crystal shapes. Another consideration is that the surface reflectance correction in (13) may be insufficient to account for the clear-sky reflectance at high viewing angles. Rayleigh scattering above and below the clouds also may be significant.

The comparison of the rms cloud heights to the ISCCP cloud heights again shows that the ISCCP approach tends to underestimate cloud height for relatively thin clouds. The lowest differences in cloud height occur for those HIRS pixels that have the highest vertical emittance.

e. Error analysis

In the previous analysis, the AVHRR pixel emittances are calculated using a cloud radiance determined from HIRS sounding channel data approximately aligned with the AVHRR pixels. The alignment is approximate for several reasons: cloud height can vary

TABLE 6. Cloud characteristics at 1930 UTC 27 October 1986 for the following viewing conditions: $\theta_0 = 60°$, $\theta = 57°$, and $\phi = 38°$. The quantities P_{cld} and Z_{cld} refer to cloud pressure and cloud height, respectively. The quantities ϵ_v^{avg} and ρ^{avg} are the average vertical emittance and average reflectance derived from the AVHRR pixels collocated with each HIRS pixel. The superscripts 6/7, rms, and ISCCP denote quantities derived using the ratio method (using HIRS channels 6 and 7), the rms method, or the ISCCP method, respectively.

HIRS pixel	Symbol	Latitude (°N)	Longitude (°W)	$P^{6/7}_{\text{cld}}$ (mb)	$Z^{6/7}_{\text{cld}}$ (km)	$P^{\text{rms}}_{\text{cld}}$ (mb)	$Z^{\text{rms}}_{\text{cld}}$ (km)	ϵ_v^{avg}	ρ^{avg}	$Z^{\text{ISCCP}}_{\text{cld}}$ (km)
1	○	44.28	91.20	200	11.8	200	11.8	0.11	0.14	3.5
2	□	44.63	91.43	200	11.8	200	11.8	0.20	0.26	5.4
3	△	44.97	91.66	200	11.8	250	10.4	0.18	0.25	6.0
4	◇	45.31	91.90	200	11.8	200	11.8	0.12	0.17	6.7
5	*	45.59	91.03	200	11.8	200	11.8	0.11	0.13	2.7

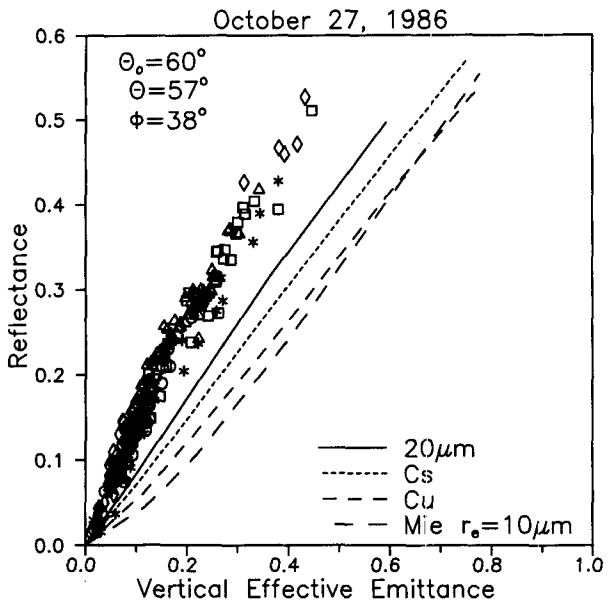

FIG. 12. Same as Fig. 8, except the data are taken from 27 October 1986 for the following viewing conditions: $\theta_0 = 60°$, $\theta = 57°$, $\phi = 38°$.

within a single 18-km HIRS footprint, the AVHRR and HIRS instruments may not be perfectly aligned (Aoki 1985), and the HIRS point-spread function is not known. The close agreement for the AVHRR and HIRS 11-μm brightness temperatures shown in Figs. 2 and 3 argue that the alignment and point-spread function uncertainties are probably minor at the 18-km scale of the HIRS pixel. Variation of cloud height within a HIRS pixel is more difficult to assess. We can, however, bound the problem with a worst-case scenario. Instead of examining cloud-height variations within the HIRS pixel, we determine the spatial variation of cloud height between adjacent HIRS pixels. HIRS pixels have a typical separation of approximately 40 km. The standard deviation of cloud height is calculated for sets of 2 × 2 HIRS pixels for the cases of 27 and 28 October 1986 and 2 November 1986, and the results are averaged over the entire region specified in section 3b. The average standard deviation in cloud height for the region is at or below 1 km for all three cases. When this standard deviation in cloud height, and thus cloud radiance, is applied to the calculation of emittances, we find that the relative error in calculated emittances is between 11% and 25%. A relative error of this magnitude will not change the results presented in Figs. 9–13.

6. Concluding remarks

The multispectral, multiresolution (MSMR) method of combining the HIRS sounding channel data with the AVHRR imaging data appears to be feasible and improves the cloud-retrieval capability using either dataset alone. The methodology developed in this study, in conjunction with ground-based instrumentation such as rawinsondes and lidar, has yielded some results that are consistent with earlier studies. The data from the FIRE-Cirrus experiment provide a unique opportunity to compare satellite measurements, surface measurements, and theoretical calculations. The conclusions from this study are:

1) The HIRS sounding channel data may be used to derive an emittance-weighted cloud fraction ϵA_{cld}. If the cloud occurs over a large scale, then ϵA_{cld} would be essentially the emittance since the cloud fraction would be one. Analysis of the 2 November 1986 data shows that many of the HIRS pixels are not completely cloud filled. In the event that the cloud fraction is not 1, then the HIRS-derived cloud pressure is used to determine an average emittance using the 11-μm data from collocated AVHRR pixels.

2) Cloud pressures retrieved using the rms and ratio methods agree within a mean of 3.0 mb and a standard deviation of 30 mb for all of the HIRS pixels that registered cloud on 27 and 28 October and 2 November 1986, at the times discussed in the text.

3) Comparison of the HIRS-derived rms cloud heights against FIRE surface and aircraft lidar data gave a mean height difference of 0.8 km with a standard deviation of 1 km, in agreement with earlier theoretical and observational studies.

TABLE 7. Cloud characteristics at 2100 UTC 28 October 1986 for the following viewing conditions: $\theta_0 = 71°$, $\theta = 48°$, and $\phi = 147°$. The quantities P_{cld} and Z_{cld} refer to cloud pressure and cloud height, respectively. The quantities ϵ_v^{avg} and ρ^{avg} are the average vertical emittance and average reflectance derived from the AVHRR pixels collocated with each HIRS pixel. The superscripts 6/7, rms, and ISCCP denote quantities derived using the ratio method (using HIRS channels 6 and 7), the rms method, or the ISCCP method, respectively.

HIRS pixel	Symbol	Latitude (°N)	Longitude (°W)	$P_{cld}^{6/7}$ (mb)	$Z_{cld}^{6/7}$ (km)	P_{cld}^{rms} (mb)	Z_{cld}^{rms} (km)	ϵ_v^{avg}	ρ^{avg}	Z_{cld}^{ISCCP} (km)
1	○	44.24	89.9	262	10.2	250	10.5	0.32	0.24	6.5
2	□	44.30	89.2	332	8.6	275	9.9	0.46	0.34	7.0
3	△	44.61	90.0	200	11.8	250	10.5	0.15	0.15	4.4
4	◇	44.67	89.3	402	7.3	453	6.4	0.17	0.17	2.9
5	*	44.98	90.1	267	10.1	275	9.9	0.38	0.32	5.0

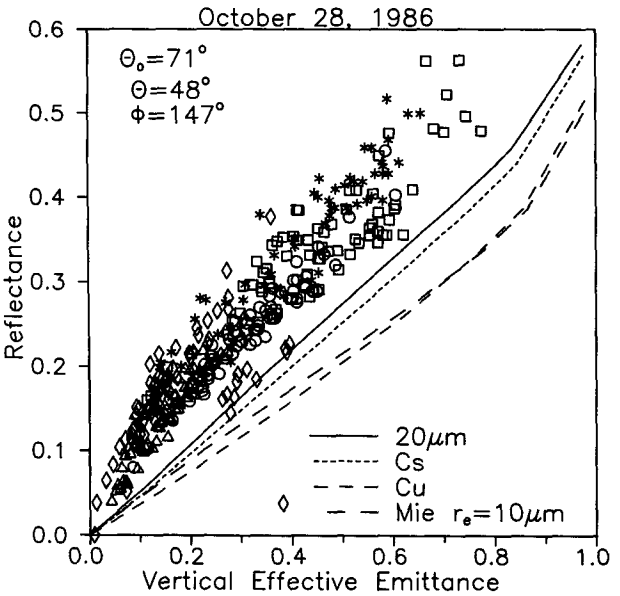

FIG. 13. Same as Fig. 8, except the data are taken from 28 October 1986 for the following viewing conditions: θ_0 = 71°, θ = 48°, ϕ = 147°.

4) Tests of cirrus reflectance–emittance relationships derived using the AVHRR radiances and HIRS cloud heights showed agreement with the results of Wielicki et al. (1990) derived independently using Landsat radiances and ER-2 lidar cloud heights. While the study of Wielicki et al. (1990) considered only a single cirrus case on 28 October 1986 for nadir viewing, the present study examines results on 27 and 28 October and 2 November for a range of viewing zenith angles between 0° and 57°. In all cases, for a given 11-μm effective vertical emittance, the measured cloud reflectance is much greater than that predicted using Mie theory (factors of 2–3) and is similar to or greater than the reflectances predicted using hexagonal ice-particle scattering phase functions (Takano and Liou 1989a). The reflectance–emittance relationships agree best with the ice-particle phase functions calculated for the Cs size distribution or for a single particle of 20-μm length. Results using the Cu size distribution underpredicted reflectance for all cases. These results are qualitatively in agreement with the study of Wielicki et al. (1990). Cirrus clouds appear to exhibit much higher sidescatter (near 90° scattering angle in the phase function) than predicted by Mie spheres or large hexagonal ice crystals (Cu).

5) There is some indication that the HIRS-derived cloud heights for large viewing zenith angles (greater than 40°) may be systematically too high. While there are an insufficient number of cases (2) to draw a general conclusion, future lidar studies should examine the dependence of HIRS-derived cloud heights on viewing zenith angle. If true, this bias might explain the larger discrepancy between observations and theory on the 27 and 28 October cases. A cloud height lower by 2–3 km would bring these results into agreement with the Cs and 20-μm ice-particle results.

6) The ISCCP method of deriving cloud height is compared with the HIRS-derived cloud heights for the HIRS pixels in Tables 3–7 for a total of 25 cases. The ISCCP cloud heights are lower than the HIRS-derived heights for all but one of these cases. The average HIRS–ISCCP cloud-height difference is 4.2 km with a standard deviation of 2.6 km. For the cases presented in this study, the use of the water-droplet phase function is not optimal for clouds composed of ice crystals; it leads to an underestimate of the true cloud height for cases when the cloud emittance is less than 1. This finding is consistent with the theoretical and empirical results of Minnis (1991). Replacement of the Mie scattering phase function with the Cs ice-particle distribution phase function from Takano and Liou (1989a) would substantially improve the ISCCP results for our test cases. However, more work needs to be done in this area since the cases presented in this study do not cover the full range of scattering angles and represent a limited set of results over a relatively small region.

The in-depth study of the small number of cases studied here provides a starting point for more extended datasets, such as the region around Bermuda for the entire month of April 1989. Bermuda was a site used in the first Surface Radiation Budget Satellite Experiment. Further work will improve the MSMR algorithm to take advantage of the other AVHRR spectral channels in an effort to gain more information about the particle phase and size, for example, and also retrieve more information on clouds that are below 3–4 km. Further work also remains to be done on the scattering properties of realistic atmospheric ice crystals.

Acknowledgments. The authors would like to thank Drs. K. N. Liou and Y. Takano of the University of Utah for making their radiative transfer model available and for providing the phase functions for the calculations. We also thank H. Woolf for providing the HIRS upwelling radiance code, D. Starr for providing the rawinsonde data, and J. D. Spinhirne for providing the ER-2 lidar cloud heights.

APPENDIX

List of Symbols

a	radius of hexagonal ice crystal
A_{cld}	cloud fraction
$B(\nu, T)$	Planck radiance
C_a	equivalent cross-sectional area
$C(L)$	length-dependent cross-sectional area
FTM	Fort McCoy

$G^{ij}(P_{cld})$	ratio of cloud signals from two different channels
I_{clear}	clear-sky satellite radiance
I_{calc}	theoretical upwelling radiance of partially cloud-filled FOV
I_{meas}	measured upwelling radiance measured by satellite
I_{cld}	theoretical upwelling radiance of black cloud measured by satellite
I_{rms}	radiance determined by rms method
MAD	Madison
$N(L)$	length-dependent particle-size distribution
L	length of hexagonal ice crystal
P	pressure
P_{cld}	cloud pressure
T_{cld}	cloud-top temperature
T_{clr}^{BB}	clear-sky brightness temperature
T_{sfc}	surface temperature
u	ozone abundance
WAU	Wausau
α_{cld}	cloud albedo
α_{clear}	clear-sky albedo
$\bar{\alpha}_{cld}$	diffuse cloud albedo
α_{g2}	surface albedo to diffuse radiation
γ	ratio of δ_{ext} to δ_{abs}
δ_{abs}	absorption optical depth
δ_{ext}	scattering optical depth
ϵ	emittance
ϵ_v	vertical emittance
θ_0	solar zenith angle
θ	satellite viewing zenith angle
μ_0	cosine of solar zenith angle
μ	cosine of viewing zenith angle
ν	wavenumber
ρ_{meas}	measured bidirectional reflectance
ρ_{g1}	surface bidirectional reflectance
σ	standard deviation of cloud height
τ	trasmittance of atmosphere between pressure level P and $P = 0$
τ_a	transmittance of atmosphere above cloud
τ_d	transmittance through cloud to surface
τ_u	transmittance between surface and satellite
$\chi_{cld}(\mu_0, \mu, \psi)$	cloud anisotropic factor
$\chi_s(\mu_0, \mu, \psi)$	surface bidirectional reflectance factor
ϕ	satellite viewing azimuthal angle
Θ	latitude
Φ	longitude

REFERENCES

Aoki, T., 1985: A method for matching the HIRS/2 and AVHRR pictures of *TIROS-N* satellites. *Tech. Proc. Second International TOVS Study Conf.*, Igls, Austria, 349–367.

Arking, A., and J. D. Childs, 1985: Retrieval of cloud cover parameters from multispectral satellite images. *J. Climate Appl. Meteor.*, **24**, 322–333.

Chahine, M. T., 1974: Remote sounding of cloudy atmospheres. I. The single cloud layer. *J. Atmos. Sci.*, **31**, 233–243.

Coakley, J. A. Jr., and F. P. Bretherton, 1982: Cloud cover from high resolution scanner data: Detecting and allowing for partially filled fields of view. *J. Geophys. Res.*, **87**, 4917–4932.

Grund, C. J., and E. W. Eloranta, 1990: The 27–28 October 1986 FIRE IFO cirrus case study: Cloud optical properties determined by high spectral resolution lidar. *Mon. Wea. Rev.*, **118**, 2344–2355.

Heymsfield, A. J., 1975: Cirrus uncinus generating cells and the evolution of cirroform clouds. Part I: Aircraft observations of the growth of the ice phase. *J. Atmos. Sci.*, **32**, 798–808.

——, and C. M. R. Platt, 1984: A parameterization of the particle size spectrum of ice clouds in terms of the ambient temperature and the ice water content. *J. Atmos. Sci.*, **41**, 846–855.

Kidwell, K. B., 1986: *NOAA Polar Orbiter Data Users Guide*. NOAA National Climatic Data Center, Satellite Data Services Division, 150 pp.

McClatchey, R. A., R. W. Fenn, J. E. A. Selby, F. E. Volz, and J. S. Garing, 1973: Optical properties of the atmosphere (3rd ed.). AFCGRL-72-0497, 113 pp. [NTIS-N73-18412]

McCleese, D. J., and L. S. Wilson, 1976: Cloud top heights from temperature sounding instruments. *Quart. J. Roy. Meteor. Soc.*, **102**, 781–790.

Minnis, P., 1991: Inference of cirrus cloud properties from satellite-observed visible and infrared radiance. Ph.D. dissertation, University of Utah, 161 pp.

——, and E. F. Harrison, 1984a: Diurnal variability of regional cloud and clear-sky radiative parameters derived from GOES data, Part I: Analysis method. *J. Climate Appl. Meteor.*, **23**, 993–1011.

——, and ——, 1984b: Diurnal variability of regional cloud and clear-sky radiative parameters derived from GOES data. Part III: November 1978 radiative parameters. *J. Climate Appl. Meteor.*, **23**, 1032–1051.

——, D. F. Young, K. Sassen, J. M. Alvarez, and C. J. Grund, 1990: The 27–28 October 1986 FIRE IFO cirrus case study: Cirrus parameter relationships derived from satellite lidar data. *Mon. Wea. Rev.*, **118**, 2402–2425.

Parker, L., and B. A. Wielicki, 1990: Comparison of satellite based cloud retrieval methods for cirrus and stratocumulus. *Proc. FIRE Science Conference*, Monterey, NASA Conference Publication 3079, 263–267.

Platt, C. M. R., D. W. Reynolds, and N. L. Abshire, 1980: Satellite and lidar observations of the albedo, emittance, and optical depth of cirrus compared to model calculations. *Mon. Wea. Rev.*, **108**, 195–204.

Rossow, W. B., L. C. Garder, P. Lu, and A. Walker, 1988: International Satellite Cloud Climatology Project (ISCCP), Documentation of cloud data. WCRP Rep. WMO/TD-No. 266, 122 pp.

Sassen, K., C. J. Grund, J. Spinhirne, M. Hardesty, and J. M. Alvarez, 1990: The 27–28 October 1986 FIRE IFO cirrus case study: A five lidar overview of cloud structure and evolution. *Mon. Wea. Rev.*, **118**, 2288–2311.

Smith, W. L., and C. M. R. Platt, 1978: Comparison of satellite-deduced cloud heights with indications from radiosonde and ground-based laser measurements. *J. Appl. Meteor.*, **17**, 1796–1802.

——, and R. Frey, 1990: On cloud altitude determinations from high resolution interferometer sounder (HIS) observations. *J. Appl. Meteor.*, **29**, 658–662.

——, H. M. Woolf, and W. J. Jacob, 1970: A regression method for obtaining real-time temperature and geopotential height profiles from satellite spectrometer measurements and its application to *Nimbus-3* SIRS observations. *Mon. Wea. Rev.*, **98**, 604–611.

Spinhirne, J. D., and W. D. Hart, 1990: Cirrus structure and radiative parameters from airborne lidar and spectral radiometer observations: The 28 October 1986 FIRE case study. *Mon. Wea. Rev.*, **118**, 2329–2343.

——, D. L. Hlavka, and W. D. Hart, 1988: ER-2 Lidar Observations from the October 1986 Fire Cirrus Experiment. NASA Tech. Memo. 100704, 49 pp.

Starr, D. O'C., and D. P. Wylie, 1990: The 27–28 October 1986 FIRE IFO cirrus case study: Meteorology and clouds. *Mon. Wea. Rev.*, **118,** 2259–2287.

Suttles, J. T., R. N. Green, P. Minnis, G. L. Smith, W. F. Staylor, B. A. Wielicki, I. J. Walker, D. F. Young, V. R. Taylor, and L. L. Stowe, 1988: Angular radiation models for earth–atmosphere system. Vol. I: Shortwave radiation. NASA Reference Publication 1184, 147 pp.

Takano, Y., and K.-N. Liou, 1989a: Solar radiative transfer in cirrus clouds. Part I: Single-scattering and optical properties of hexagonal ice crystals. *J. Atmos. Sci.*, **46,** 3–19.

——, and ——, 1989b: Solar radiative transfer in cirrus clouds. Part II. Theory and computation of multiple scattering in an anisotropic medium. *J. Atmos. Sci.*, **46,** 20–36.

Weinreb, M. P., H. E. Fleming, L. M. McMillin, and A. C. Neuendorffer, 1981: Transmittances for the TIROS operational sounder, NOAA Tech. Rep. NESS 85, 60 pp.

Whitlock, C. H., W. F. Staylor, J. T. Suttles, G. L. Smith, R. Levin, R. Frouin, C. Gautier, P. M. Teillet, P. N. Slater, Y. J. Kaufman, B. N. Holben, W. B. Rossow, C. Brest, and S. R. LeCroy, 1990: AVHRR and VISSR satellite instrument calibration results for both cirrus and marine stratocumulus IFO periods. NASA CP 3083, 141–146.

Wielicki, B. A., and J. A. Coakley, Jr., 1981: Cloud retrieval using infrared sounder data: Error analysis. *J. Appl. Meteor.*, **20,** 157–169.

——, and R. M. Welch, 1986: Cumulus cloud field properties derived using Landsat digital data. *J. Climate Appl. Meteor.*, **24,** 539–546.

——, J. T. Suttles, A. J. Heymsfield, R. M. Welch, J. D. Spinhirne, M. L. C. Wu, D. Starr, L. Parker, and R. F. Arduini, 1990: The 27–28 October 1986 FIRE IFO cirrus case study: Comparison of radiative transfer theory with observations by satellite and aircraft. *Mon. Wea. Rev.*, **118,** 2356–2376.

Wylie, D. P., and W. P. Menzel, 1989: Two years of cloud cover statistics using VAS. *J. Climate,* **2,** 380–392.